Global-Gyrokinetic Study of Finite β Effects on Linear Microinstabilities

G.L. Falchetto,* J. Vaclavik, and L. Villard

Centre de Recherches en Physique des Plasmas,

Association Euratom-Confédération Suisse,

Ecole Polytechnique Fédérale de Lausanne,

CRPP-PPB, CH-1015 Lausanne, Switzerland

(Dated: November 27, 2002)

Abstract

Electromagnetic microinstabilities in tokamak plasmas are studied by means of a linear global eigenvalue numerical code. Ion dynamics is described by the gyrokinetic equation, so that finite ion Larmor radius effects are taken into account to all orders. Non adiabatic electrons are included in the model, with passing particles described by the drift-kinetic equation and trapped particles through the bounce averaged drift-kinetic equation. A large aspect ratio plasma with circular shifted surfaces is considered for the numerical implementation. The effects of an electromagnetic perturbation on toroidal Ion Temperature Gradient driven (ITG) modes are studied, confirming the stabilization of these modes with increasing β (parameter identifying the ratio of the plasma pressure to the magnetic pressure). The threshold for the destabilization of an electromagnetic mode, the so-called kinetic ballooning mode (KBM) or Alfvénic Ion Temperature Gradient mode (AITG) is identified. Moreover, owing to the global formulation, the radial structure of these electromagnetic modes is observed for the first time. Finally, the contributions of trapped electron dynamics and the effects of the Shafranov shift are addressed.

PACS numbers: 52.30.Gz, 52.65.Tt, 52.35.Qz, 52.35.Hr, 02.70.Hm

*Present address: Association Euratom-CEA, DRFC/DSM, CEA Cadarache, 13108 St. Paul-lez-Durance, Cedex, France; E-mail: gloria.falchetto@cea.fr

I. INTRODUCTION

The key role of magnetic fluctuations, also called finite β effects, in the study of microinstabilities has been identified by numerous authors. Magnetic fluctuations have a strong impact on magnetized plasmas, both altering the dynamics of predominantly electrostatic instabilities and introducing new electromagnetic modes. This has motivated the development in recent years of several different models, either fluid or kinetic or hybrid MHD-kinetic, for the study of electromagnetic microinstabilities in tokamak plasmas. These different approaches agree qualitatively in showing that the main effect of finite β consists in the stabilization of the collisionless toroidal Ion Temperature Gradient (ITG) driven modes and in the destabilization, above a certain β value, of a new branch of electromagnetic modes. These modes, having frequency higher than the ITG's but lower than the Alfvén waves, have been called either kinetic ballooning modes (KBM)[1],[2] or shear-Alfvénic Ion Temperature Gradient modes (AITG) [3], referring to one or more of the salient characteristics of this instability. The theory of kinetic ballooning modes in general geometry was first introduced in [1] as a procedure to study the influence of kinetic effects on the stability of MHD ballooning modes. The so-called kinetic ballooning modes were shown to be destabilized by kinetic effects such as trapped particles and temperature gradients, when the plasma β is above a certain threshold. The threshold was initially identified to be near the critical β value for the MHD stability of ballooning modes [4]. Nonetheless a more quantitative description of microinstabilities has been assessed to require the exact treatment of microscopic features, such as resonances [5, 6] and finite Larmor radius (FLR) effects [7], as well as of toroidal effects [3],[8]. Therefore gyrokinetic simulations being able to deal with toroidal geometry and non-adiabatic electron dynamics are essential to provide an insight on finite β instabilities in the low-frequency regime. Furthermore, since the non-linear gyrokinetic study of electromagnetic fluctuations is hindered by the difficulty of treating the dynamics of electrons, linear gyrokinetic simulations represent now a useful tool and can provide benchmark to non-linear computations. Substantial progress in linear electromagnetic gyrokinetic simulations has been achieved in the past few years. In [5] and [3, 8] use is made of the ballooning representation, ions are treated as gyrokinetic while for non-adiabatic electrons use is made of the frequency ordering $\omega \ll |k_\parallel v_{the}|$; the Shafranov shift is taken into account by means of the "$s-\alpha$" model, [9], whereas all trapped particle dynamics is neglected. Results from

truly global eigenvalue electromagnetic simulations have been obtained using the code KIN-2DEM [10], based on a second order expansion with respect to the banana width which, alas, leads to the presence of lots of spurious modes in the spectra. The eigenvalue problem is there reduced to a coupled ordinary differential equation system in the radial direction, which is solved by a finite element method, using the algorithm developed in [11]; a Fourier decomposition is used in the poloidal direction. Both passing ion dynamics and Shafranov shift effects are neglected there.

In light of the problems outlined above, a global gyrokinetic study including all the important effects related to toroidicity, parallel ion dynamics, non-adiabatic electron dynamics, finite Larmor radius(FLR), trapped particles and equilibrium effects, appears necessary to a complete understanding of electromagnetic drift-waves. All the mentioned effects are accounted for in the work presented here, which aims to analyze the electromagnetic effects on microinstabilities, in the framework of linear gyrokinetic theory, by means of a 2D global representation. More precisely, this work has involved the implementation of electromagnetic effects in the electrostatic global gyrokinetic spectral toroidal code, GLOGYSTO [12, 13]. Non-adiabatic passing electron dynamics and the Shafranov shift have furthermore been implemented. The eigenvalue problem is solved in a special Fourier space adapted to the curved geometry, which allows one to keep orbit width and Larmor radius effects to all orders and thus avoids the introduction of non-physical modes. The model is applied to a collisionless, finite β plasma, represented through an axisymmetric, large aspect ratio tokamak equilibrium with circular shifted magnetic surfaces. The model is bi-dimensional and global, the electromagnetic system of equations being solved on the whole poloidal section. Section II presents the linear global electromagnetic gyrokinetic formulation first in a general geometry, then in the limit of a large aspect ratio tokamak. The following subsections describe the solution of the electromagnetic gyrokinetic equation in this approximation for the two particle species, ions and electrons, besides distinguishing between circulating and trapped particles. The implementation of the Shafranov shift is described in section II A 4. Section III contains a discussion on the numerical implementation of the global electromagnetic code. Section IV gathers the global simulations results; the effect of finite β on the stability of ITG modes and of the new appearing electromagnetic modes, is studied by means of various parameter scans, together with trapped electron dynamics and Shafranov shift. Mode structures are shown of the so-called AITG or kinetic ballooning modes. In section V

conclusions are drawn on the presented work and proposals for future developments are outlined.

II. FORMULATION

In this section the derivation of the electromagnetic gyrokinetic equation is provided, for the general case of an axisymmetric toroidal system. The usual gyrokinetic ordering is adopted, $\omega/\omega_{ci} \sim k_\parallel/k_\perp \sim \mathcal{O}(\epsilon)$ and $k_\perp \rho_{Li} \sim \mathcal{O}(1)$, having defined the small parameter $\epsilon \doteq \rho_{Li}/L$, ratio of the ion Larmor radius $\rho_{Li} = v_{thi}/\omega_{ci}$ to a typical scale length of the system. In the previous, ω is the characteristic mode frequency, $\omega_{ci} = q_i B/m_i$ the ion cyclotron frequency, $k_\parallel$ and $k_\perp$ are the components of the wavevector parallel and perpendicular to the magnetic field .

A general derivation of the linearized electromagnetic gyrokinetic equation was given by Catto *et al.* [14]. In the present work a low, but still finite, β plasma is considered, therefore the perturbed magnetic field can be described in terms of the only parallel component of the vector potential, taking the gauge $\vec{A_\perp} = 0$; this means that in this model the perturbations of the magnetic field parallel to the field lines are neglected, $\delta B_\parallel = 0$. The plasma is described by means of a system of two equations, namely the quasi-neutrality equation and the parallel component of Ampère's law:

$$\sum_j \int d\vec{v}\ \tilde{f}_j(\vec{r},\vec{v},\omega) = 0\,; \tag{1}$$

$$\nabla^2{}_\perp\, A_\parallel = \frac{4\pi}{c} \sum_j q_j \int d\vec{v}\ v_\parallel\ \tilde{g}_j(\vec{r},\vec{v},\omega)\ ; \tag{2}$$

where $\tilde{g_j}$ is the non-adiabatic part of the perturbed distribution function $\tilde{f_j}$, for each species j of particles, which is derived as the solution of the electromagnetic gyrokinetic equation . Applying a small electromagnetic perturbation to the equilibrium plasma, the distribution function can be expressed as the sum of a fluctuating part and an unperturbed distribution function F:

$$f = \tilde{f} + F(\mathcal{E},\mu,\psi_0)\,; \tag{3}$$

where F is defined as a function of the energy $\mathcal{E} = v^2/2$, the magnetic moment $\mu = v_\perp^2/2B$ and the canonical momentum conjugated to the toroidal velocity, $\psi_0 = \psi + (mr/q)\ \vec{v}\cdot\vec{e_\varphi}$,

ψ being the poloidal flux and $\vec{e}_\varphi$ the toroidal direction.

Vlasov equation can then be linearized with respect to the small electromagnetic perturbation of the equilibrium state, besides expliciting the electric and magnetic field in terms of the electrostatic potential ϕ and the parallel vector potential $A_\parallel$. The following expression is obtained, at the lowest order in the gyro-ordering:

$$\begin{aligned}\left.\frac{D}{Dt}\right|_{u.t.}\tilde{f} \;=\; & \frac{q}{m}\,\vec{v}\cdot\left\{\nabla\phi\left[\left(1-\frac{v_\varphi}{\Omega_p}\,\nabla_n\right)\frac{\partial F}{\partial\mathcal{E}}+\frac{1}{B}\frac{\partial F}{\partial\mu}\right]-\nabla A_\parallel\,\frac{v_\parallel}{cB}\,\frac{\partial F}{\partial\mu}\right\}\\ & -\frac{q}{m}\nabla\phi\left(\vec{e_\parallel}\,\frac{v_\parallel}{B}\,\frac{\partial F}{\partial\mu}+\vec{e_\varphi}\,\frac{1}{\Omega_p}\nabla_n F\right)+\frac{q}{mc}\,\frac{\partial A_\parallel}{\partial t}\,v_\parallel\,\frac{\partial F}{\partial\mathcal{E}} \qquad (4)\\ & +\frac{q}{mc}\,\left\{\frac{v_\parallel}{B}\,\frac{\partial F}{\partial\mu}\,\nabla_\parallel(v_\parallel A_\parallel)+\left(\vec{v}\times(\nabla\times\vec{A_\parallel})\right)_\varphi\frac{1}{\Omega_p}\nabla_n F\right\}+\mathcal{O}(\epsilon);\end{aligned}$$

the left hand side represents the total derivative of the fluctuating distribution function, evaluated over the unperturbed particle trajectories. In the above expression terms of the first order in transport ordering, i.e. $\partial/\partial\mu \ll \partial/\partial\mathcal{E}$ have been neglected. Use is made of the relation $\nabla_n = -rB_p\,\partial/\partial\psi_0$; $\Omega_p \doteq \omega_c B_p/B$, where $\omega_c = qB/m$ is the cyclotron frequency and B_p is the poloidal component of the magnetic field, and $\vec{e}_\parallel$ the magnetic field lines direction. One can define a new distribution function via:

$$\tilde{f} = h + \phi\,\frac{q}{m}\left[\left(1-\frac{v_\varphi}{\Omega_p}\,\nabla_n\right)\frac{\partial F}{\partial\mathcal{E}}\right]+\frac{q}{mB}\frac{\partial F}{\partial\mu}\left(\phi-\frac{v_\parallel}{c}\,A_\parallel\right); \qquad (5)$$

such that equation (4) can be rewritten as follows,

$$\begin{aligned}\left.\frac{D}{Dt}\right|_{u.t.} h \;\cong\; & -\frac{q}{m}\frac{\partial}{\partial t}\left(\phi-\frac{v_\parallel}{c}\,A_\parallel\right)\frac{\partial F}{\partial\mathcal{E}}-\frac{q}{m}\frac{v_\parallel}{B}\,\frac{\partial F}{\partial\mu}\,\nabla_\parallel\left(\phi-\frac{v_\parallel}{c}\,A_\parallel\right)\\ & -\frac{q}{m}\frac{\nabla_n F}{\Omega_p}\left[\nabla\phi-\frac{1}{c}\,\left(\vec{v}\times(\nabla\times\vec{A_\parallel})\right)\right]_\varphi\\ =\; & \frac{q}{m}\left(\frac{\partial F}{\partial\mathcal{E}}\,\frac{\partial}{\partial t}+\frac{v_\parallel}{B}\,\frac{\partial F}{\partial\mu}\,\nabla_\parallel+\frac{\nabla_n F}{\Omega_p}\,\nabla_\varphi\right)\left(\frac{v_\parallel}{c}\,A_\parallel-\phi\right). \qquad (6)\end{aligned}$$

To obtain the gyrokinetic equation , first a transformation to gyrocenter variables is performed, then the equation is averaged over the gyroangle.

Finally, the electromagnetic gyrokinetic equation in gyrocenter coordinates, for a general axisymmetric system, at the lowest order in the gyrokinetic parameter, reads

$$\left(\frac{\partial}{\partial t}+\vec{v_g}\cdot\frac{\partial}{\partial\vec{x_g}}\right)h=\frac{q}{m}\left(\frac{\partial F}{\partial\mathcal{E}}\,\frac{\partial}{\partial t}+\frac{v_\parallel}{B}\,\frac{\partial F}{\partial\mu}\,\nabla_\parallel+\frac{\nabla_n F}{\Omega_p}\,\nabla_\varphi\right)\langle\,\frac{v_\parallel}{c}\,A_\parallel-\phi\,\rangle_\alpha. \qquad (7)$$

The LHS represents the total time derivative along unperturbed gyrocenter trajectories, the gyrocenter velocity is expressed as $\vec{v_g} = \vec{v_\parallel} + \vec{v_d}$, with $\vec{v_d} = \frac{1}{\omega_c}\left(v_\perp^2/2 + v_\parallel^2\right)\vec{e_\parallel} \times \nabla \ln B$, the drift velocity due to the gradient and curvature of the magnetic field, while the gyrocenter position is given by $\vec{x_g} = \vec{r} + (\vec{v} \times \vec{e_\parallel})/\omega_c$. The brackets $\langle \quad \rangle_\alpha$ stand for the average over the gyroangle, α, which can easily be performed taking advantage of a Fourier transform of both potentials in the perpendicular direction

$$A_\parallel(\vec{r}) = \int d\vec{k_\perp}\ \hat{A}_\parallel(\vec{k_\perp}, \vec{x}_{g\parallel}) \exp\left[i\vec{k_\perp} \cdot \left(\vec{x}_g - \frac{\vec{v} \times \vec{e_\parallel}}{\omega_c}\right)\right]\ ; \tag{8}$$

hence

$$\langle A_\parallel \rangle_\alpha = \int d\vec{k_\perp}\ \hat{A}_\parallel(\vec{k_\perp}, \vec{x}_{g\parallel})\ J_0\left(\frac{k_\perp v_\perp}{\omega_c}\right) e^{i\vec{k_\perp}\cdot\vec{x}_g}; \tag{9}$$

where use has been made of the integral form of Bessel function J_0.

1. *Solution to the electromagnetic gyrokinetic equation*

For the sake of simplicity, the unperturbed distribution function is chosen to only depend on the energy and the poloidal flux; furthermore, the plasma is assumed to be close to a local equilibrium, thus the distribution function F will be a Maxwellian $F_M(\mathcal{E}, \psi) = N/(2\pi(T/m))^{3/2}\ \exp\{-\mathcal{E}/(T/m)\}$, $N(\psi)$ and $T(\psi)$ being the density and temperature at a given magnetic surface. Replacing the Maxwellian in (7), one obtains

$$\left.\frac{D}{Dt}\right|_{u.t.g.} h = -\frac{q}{T} F_M \left[\frac{\partial}{\partial t} + \frac{T}{qB}\nabla_n \ln F_M\ \nabla_b\right] \langle\ \frac{v_\parallel}{c}\ A_\parallel - \phi\ \rangle_\alpha\,; \tag{10}$$

where use was made of $(B/B_p)\nabla_\varphi \simeq -\nabla_b + \mathcal{O}(\epsilon)$. The solution to this electromagnetic gyrokinetic equation is derived considering a perturbation having a time dependence $e^{-i\omega t}$:

$$h = -\frac{q}{T}\ F_M \int d\vec{k}\ J_0\left(\frac{k_\perp v_\perp}{\omega_c}\right) e^{i\vec{k}\cdot\vec{x}_g}\ (\omega - \omega^*)\ i\,\mathcal{P}\left(\hat{\phi}(\vec{k}) - \frac{v_\parallel}{c}\ \hat{A}_\parallel(\vec{k})\right); \tag{11}$$

where one defined $\omega^* \doteq \frac{T}{qB}\ (\nabla_n \ln F_M)\ k_b$, the diamagnetic drift frequency ; whereas $\mathcal{P}$ is the propagator, representing the time integral of the phase factor of a given wave component

$$\mathcal{P}(\vec{k}, t) \equiv \int_{-\infty}^{t} dt'\ \exp\left[i\left(\int_t^{t'} dt''\ \vec{k} \cdot \vec{v_g}(t'') - \omega t'\right)\right]. \tag{12}$$

The solution to the gyrokinetic equation is provided by solving for this propagator, which comes down to solve for the trajectories of gyrocenters. A further development of the propagator, useful for numerical implementation, is carried on by using an approach originally derived in [15]. One can define a function representing the spatial phase in (12)

$$g(t) = \int_0^t \vec{k} \cdot \vec{v_g}\, dt' \; ;$$

remarking that this phase is generally not periodic in time, one can explicitly subtract the secular term and define a periodic function $\tilde{g}$, satisfying $\tilde{g}(\tau) = 0$

$$g(t) = \bar{\omega} t + \tilde{g}(t), \quad \bar{\omega} = \frac{1}{\tau} \oint \vec{k} \cdot \vec{v_g}\; dt \; . \tag{13}$$

The exponential of this function is finally decomposed into a Fourier series,

$$e^{i\,\tilde{g}(t)} = \sum_p a_p \; e^{i\,\omega_\tau\, p\, t} \; ; \qquad a_p = \frac{1}{\tau} \oint dt \; e^{i\,(\tilde{g} - p\,\omega_\tau t)} \; , \tag{14}$$

where $\omega_\tau = 2\pi/\tau$, is the frequency of the periodic motion of period τ. Introducing the previous definitions in (12), the propagator can be cast into the form:

$$\begin{aligned} \mathcal{P} \; &= \; e^{-i\,g(t)} \int_{-\infty}^{t} dt' \; e^{i(\,g(t') - \omega t')} \equiv e^{-ig(t)} \sum_p a_p \; \int_{-\infty}^{t} dt' \; e^{i(\,\bar{\omega} + p\,\omega_\tau - \omega)t'} \\ &\equiv \; e^{-i\,g(t)} \sum_p \; a_p \; \frac{e^{i(\bar{\omega} + p\,\omega_\tau - \omega)t}}{i\,(\bar{\omega} + p\,\omega_\tau - \omega)} \, . \end{aligned}$$

Finally:

$$e^{i\,\omega\,t}\; \mathcal{P} \equiv i\; e^{-i\,\tilde{g}(t)} \sum_p \frac{a_p\; e^{i\,p\,\omega_\tau t}}{\omega - \bar{\omega} - p\,\omega_\tau} \equiv i \sum_{p,\,p'} \; \frac{a_p\, a^*_{p'}\; e^{i\,(p - p')\,\omega_\tau t}}{\omega - \bar{\omega} - p\,\omega_\tau} \, . \tag{15}$$

One can remark that the possible resonances with the frequency ω_τ and its harmonics appear now explicitly.

To evaluate the charge density and the parallel current, one has to transform back (11) to particle variables and integrate the perturbed distribution function $\tilde{f}$ over velocity space:

$$\tilde{n}(\vec{r}) = -\frac{qN}{T} \left[\phi + \int d\vec{k}\; e^{i\vec{k}\cdot\vec{r}} \int d\vec{v}\; J_0^2 \left(\frac{k_\perp\, v_\perp}{\omega_c} \right) \frac{F_M}{N}\; (\omega - \omega^*) i\mathcal{P} \left(\phi(\vec{k}) - \frac{v_\parallel}{c}\; A_\parallel(\vec{k}) \right) \right] ; \tag{16}$$

$$q \int d\vec{v}\; v_\parallel\; h = -\frac{q^2}{T} \; \int d\vec{k}\; e^{i\vec{k}\cdot\vec{r}} \; \int d\vec{v}\; v_\parallel\; J_0^2 \left(\frac{k_\perp v_\perp}{\omega_c} \right) \; F_M(\omega - \omega^*)\; i\mathcal{P} \; \left(\hat{\phi}(\vec{k}) - \frac{v_\parallel}{c} \hat{A}_\parallel(\vec{k}) \right) . \tag{17}$$

where $\int d\vec{v} \equiv 2\pi \int_{-\infty}^{\infty} dv_\parallel \int_0^\infty dv_\perp v_\perp$ and the gyroangle integration has been performed providing a second Bessel function J_0.

2. Eigenvalue system in Fourier representation

The system (1) and (2), is finally solved in Fourier space, projecting both the density and the parallel current on $\exp\{i\vec{k}\cdot\vec{r}\}$:

$$\sum_j \tilde{n}_j(\vec{k}) = \sum_j \int d\vec{r}\, e^{-i\vec{k}\cdot\vec{r}}\, \tilde{n}_j(\vec{r})$$

$$\equiv \sum_j \int d\vec{k'} \left[\mathcal{M}_{\phi\phi}{}^j(\vec{k},\vec{k'})\, \hat{\phi}(\vec{k'}) + \mathcal{M}_{\phi A}{}^j(\vec{k},\vec{k'}) \hat{A}_\parallel(\vec{k'}) \right] = 0\,; \qquad (18)$$

$$\int d\vec{r}\, e^{-i\vec{k}\cdot\vec{r}}\, \nabla_\perp^2 \hat{A}_\parallel(\vec{r}) = \frac{4\pi}{c} \sum_j j_{\parallel_j}(\vec{k})$$

$$\equiv \sum_j \int d\vec{k'} \left[\mathcal{M}_{A\phi}{}^j(\vec{k},\vec{k'})\, \hat{\phi}(\vec{k'}) + \mathcal{M}_{AA}{}^j(\vec{k},\vec{k'}) \hat{A}_\parallel(\vec{k'}) \right]. \qquad (19)$$

The above system of two equations can be represented by the equivalent matrix form

$$\begin{pmatrix} \mathcal{M}_{\phi\phi} & \mathcal{M}_{\phi A} \\ \mathcal{M}_{A\phi} & \mathcal{M}_{AA} \end{pmatrix} \begin{pmatrix} \hat{\phi} \\ \hat{A}_\parallel \end{pmatrix} = 0\,; \qquad (20)$$

where each of the submatrices is a sum over the contributions from the different particle species; besides the LHS of Ampère's law is included in $\mathcal{M}_{AA} \equiv \mathcal{M}_{AA}{}^{\nabla^2} + \mathcal{M}_{AA}{}^{ion} + \mathcal{M}_{AA}{}^{el.}$.

A. Large aspect ratio tokamak

The above general formulation has been applied for numerical implementation to the case of a large aspect ratio tokamak, with circular, concentric magnetic surfaces. In this case the plasma is confined by a magnetic field of the form:

$$\vec{B} = B_0 \frac{R}{r} \left(-\frac{\rho}{q_s R}\, \vec{e_\theta} + \vec{e_\varphi} \right) \qquad (21)$$

where R is the major radius, ρ the toroidal radial coordinate, $r = R + \rho\cos\theta$ the cylindrical radial coordinate and $q_s(\rho) = |\rho B_\varphi / R B_\theta|$ the safety factor. Applying the large aspect ratio geometry approximation one retains only the lowest order terms with respect to the inverse aspect ratio, $\varepsilon \doteq \rho/R$. The explicit expression of the propagator for each particle species and the corresponding submatrices, referring to (20), are derived in the following subsections. Remark that the modification of gyrocenter trajectories due to the Shafranov

shift is taken into account in a second stage, in subsection II A 4. Note that in all this section the international system of units (SI) is used and the parallel vector potential is normalized with respect to the ion thermal velocity on axis $v_{thi}(0)$.

The electrostatic and parallel vector potentials are in this case represented through a discrete Fourier transform both in the radial and poloidal direction, by means of a decomposition adapted to the toroidal geometry,

$$A_\parallel(\rho,\theta,\varphi;t) = e^{i\,(n\varphi-\omega t)} \sum_{(k,m)} \hat{A}_{\parallel\,(k,m)} e^{i(\kappa\rho+m\theta)}\ ; \tag{22}$$

the toroidal wave number n is fixed owing to the axisymmetry and the local wave vector reads $\vec{k} = \kappa\,\vec{e}_\rho + k_\theta\,\vec{e}_\theta + k_\varphi\,\vec{e}_\varphi$, with $\kappa = k\,2\pi/\Delta\rho\,, k_\theta = m/\rho$ and $k_\varphi = n/R$, $\Delta\rho = \rho_u - \rho_l$ being the width of the considered radial interval. The left hand side of the parallel component of Ampère's law is then evaluated by first Fourier transforming the parallel vector potential and then applying the Laplacian operator, approximated to the lowest order in the inverse aspect ratio,

$$\nabla^2{}_\perp\, A_\parallel = \sum_{(k,m)} -\left(\kappa^2 + \frac{m^2}{\rho^2}\right)\, \hat{A}_{\parallel\,(k,m)} e^{i\,(\kappa\rho+m\theta+n\varphi)}\ ; \tag{23}$$

the submatrix acting over $\hat{A}_\parallel$ is finally obtained by projecting the LHS of the parallel component of Ampère's law on $\exp\{i\vec{k}\cdot\vec{r}\}$:

$$\mathcal{M}_{AA}{}^{\nabla^2} = -\,\frac{1}{\Delta\rho}\int_{\rho_l}^{\rho_u} d\rho\; e^{-i(\kappa-\kappa')\rho}\; \frac{T_e}{q^2\,\mu_0\,N\,v_{thi}^2(0)} \left(\kappa^2\,\delta_k^{k'} + \frac{m'^2}{\rho^2}\right) \delta_m^{m'}\,. \tag{24}$$

1. Passing ions

For passing particles the parallel velocity is considered as a constant $v_\parallel(t) = v_\parallel(t_0)$, thus the modulation of velocities along a given trajectory, due to the variations of the magnetic field, are neglected. One has to solve for the gyrocenter trajectories, which as long as the Shafranov shift is neglected, are the same as in the electrostatic case [13].

The contributions of circulating ions to the total matrix can be expressed through:

$$\mathcal{M}_{\phi\phi}{}^{ion} \;=\; \frac{1}{\Delta\rho}\int_{\rho_l}^{\rho_u} d\rho\; e^{-i(\kappa-\kappa')\rho}\,\tau\,\left\{\alpha_P\,\delta_m^{m'} + e^{i\,(m-m')\,\bar{\theta}}\;\mathcal{I}^{\,0\;ion}\right\}\ ; \tag{25}$$

$$z_i\;\mathcal{M}_{\phi A}{}^{ion} = \mathcal{M}_{A\phi}{}^{ion} \;=\; -\,\frac{1}{\Delta\rho}\int_{\rho_l}^{\rho_u} d\rho\; e^{-i(\kappa-\kappa')\rho}\; e^{i\,(m-m')\bar{\theta}}\;\tau\,\mathcal{I}^{\,1\;ion}\,; \tag{26}$$

$$\mathcal{M}_{AA}{}^{ion} \;=\; \frac{1}{\Delta\rho}\int_{\rho_l}^{\rho_u} d\rho e^{-i(\kappa-\kappa')\rho}\; e^{i\,(m-m')\bar{\theta}}\;\tau\,\mathcal{I}^{\,2\;ion}\,. \tag{27}$$

The first term in matrix ${\mathcal{M}_{\phi\phi}}^{ion}$ comes from the adiabatic ion contribution, which is weighted by the fraction of passing particles $\alpha_P = 1 - \sqrt{\varepsilon/(1+\varepsilon)}$ [12]. ${\mathcal{I}}^{l\ ion}$ represent the parallel velocity integrals, which are expressed as follows,

$$
{\mathcal{I}}^{l=0,1,2\ ion} = \frac{1}{\sqrt{2\pi}} \left(\frac{v_{thi}}{v_{thi}(0)} \right)^l
\int_{-\infty}^{\infty} dv_\parallel \, v_\parallel^l \, e^{-\frac{v_\parallel^2}{2}} \sum_p \frac{\frac{\eta_i}{2}\,\omega_{ni}\,{\mathcal{I}}^{1}_{v_\perp} - \left[\omega - \omega_{ni}\left(1 + \frac{\eta_i}{2}(v_\parallel^2 - 3)\right)\right]{\mathcal{I}}^{0}_{v_\perp}}{\omega - (n q_s - m' - p)\,\bar{\omega}_{ti}\,v_\parallel} \Bigg|_{p'=p-m+m'} . \quad (28)
$$

In the expressions above, $\tau \doteq T_e/T_i$, $\bar{\theta} \doteq \arctan(-\kappa/k_\theta)$, z_i is the atomic number, $\eta_i = d\ln T_i \,/\, d\ln N$, $\omega_{ni} = -T_i k_\theta/(q_s\, B\, |L_n|)$ is the diamagnetic frequency, L_n being the density scale length, and $\bar{\omega}_{ti} \doteq v_{thi}/q_s R$ is the average ion transit frequency. The integrals over perpendicular velocity ${\mathcal{I}}_{v_\perp}(\rho, k_\perp \rho_{Li}, v_\parallel, p, p')$ are the same as in the electrostatic case [page 3935][13], still we report them for completeness.

$$
{\mathcal{I}}^{\nu=0,1}_{v_\perp}(\rho, k_\perp\rho_{Li}, v_\parallel, p, p') = \int_0^{v_{\perp\,max}} dv_\perp \, v_\perp^{2\nu+1} \, e^{-\frac{v_\perp^2}{2}} \, J_0^2(k_\perp \rho_{Li}\, v_\perp)\, J_p(x_{ti})\, J_{p'}(x'_{ti}) \, , \quad (29)
$$

with $x_{ti} = k_\perp v_{dz}/\omega_t$, $v_{dz} = \left(v_\perp^2/2 + v_\parallel^2\right)/(\omega_{ci}\, R)$ being the ion drift velocity and $\omega_t = v_\parallel/(q_s\, R)$ the transit frequency. Note that the integration is only performed over the velocity space of circulating particles, $v_\perp < v_\parallel/\sqrt{B_{max}/B_0 - 1} \equiv v_\parallel/\sqrt{\varepsilon}$. In the expressions above velocities are normalized with respect to the ion thermal velocity $v_{thi} = \sqrt{T_i/m_i}$.

2. Passing electrons

A major modification introduced by the electromagnetic effects is the inclusion of the dynamics of non-adiabatic passing electrons, since these particles carry the dominant current perturbations which drive magnetic fluctuations.

In this model circulating electrons are considered as quasi-adiabatic, meaning that the non-adiabatic electron contribution to matrix ${\mathcal{M}_{\phi\phi}}^{el.}$ is negligible, therefore

$$
{\mathcal{M}_{\phi\phi}}^{el.} = \frac{1}{\Delta\rho} \int_{\rho_l}^{\rho_u} d\rho \, e^{-i(\kappa-\kappa')\rho} \, \alpha_P \, \delta_m^{m'} , \quad (30)
$$

where α_P is the fraction of circulating particles. Furthermore use is made of the drift-kinetic approximation and of the frequency ordering $\omega \sim \omega_{ne} \ll \bar{\omega}_{te}$, where ω_{ne} and $\bar{\omega}_{te}$ respectively stand for the electron diamagnetic frequency and the average electron transit

frequency. Remark that, owing to the considered frequency ordering, the magnetic drift will be retained only in ${\mathcal{M}_{AA}}^{el.}$.

The propagator has an explicit expression similar to the one for circulating ions:

$$\mathcal{P} = \sum_{p=0,\pm 1} J_p\left(k_\perp v_{dz}/\omega_t\right)\, J_{p'}\left(k_\perp v_{dz}/\omega_t\right)\, \frac{\exp\left[i\,(p-p')(\theta+\bar{\theta})\right]}{i\left(k_\parallel v_\parallel - p\,\omega_t - \omega\right)}\Bigg|_{p'=p-m+m'} \quad ; \tag{31}$$

where in this case $k_\perp v_{dz}/\omega_t \equiv -k_\perp\,\rho_{Le}\,q_s\,(v_{thi}/v_{the})(v_\perp^2/2+v_\parallel^2)/v_\parallel$, $\rho_{Le} \doteq v_{the}/\omega_{ce}$ being the electron Larmor radius and velocities being normalized to v_{thi} ; $k_\parallel = (nq_s - m)/(Rq_s)$. Remark that since the electron transit frequency is much higher than the frequencies of the modes under study, one has retained just its lower harmonics, $p = 0, \pm 1$; therefore there is a coupling only between neighboring poloidal numbers, because of the relation $m' = m+p-p'$. Furthermore, one takes advantage of an expansion of the Bessel functions in their small argument, $J_0\left(k_\perp v_{dz}/\omega_t\right) \sim 1$, $J_{\pm 1}\left(k_\perp v_{dz}/\omega_t\right) \sim \pm\frac{1}{2}\left(k_\perp v_{dz}/\omega_t\right)$, approximation which is consistent with the frequency ordering and enables to perform analytically the integration over perpendicular velocity. Remark that this expansion gives rise to a different dependence on drift velocity of the terms $p = p' = 0$ and the terms $p = \pm 1, p' = 0$ (or $p' = 0, p = \pm 1$). One would like to point out that for an analysis of ITG modes further approximations to the treatment of electron dynamics can be used [16](i.e. expansion of the denominator of the propagator (31) in terms of ω/ω_{te} and $k_\parallel \simeq 1/q_s\,R$), nonetheless, for the study of the electromagnetic modes, it is crucial to solve for the complete resonant propagator.

The other contributions of non-adiabatic electrons to the matrix read:

$${\mathcal{M}_{\phi A}}^{el.} = {\mathcal{M}_{A\phi}}^{el.} \;=\; -\,\frac{1}{\Delta\rho}\int_{\rho_l}^{\rho_u} d\rho\; e^{-i(\kappa-\kappa')\rho}\;\alpha_P\;{\mathcal{I}}^{\,1\;el.}\;\delta_m^{m'}\;; \tag{32}$$

$${\mathcal{M}_{AA}}^{el.} \;=\; \frac{1}{\Delta\rho}\int_{\rho_l}^{\rho_u} d\rho\; e^{-i(\kappa-\kappa')\rho}\; e^{i\,(m-m')\bar{\theta}}\;\alpha_P\;{\mathcal{I}}^{\,2\;el.}\;. \tag{33}$$

The parallel velocity integrals are defined as,

$${\mathcal{I}}^{\,l\;el.} = \left(\frac{v_{thi}}{v_{thi}(0)}\right)^l\;\left(\frac{v_{thi}}{v_{the}}\right)\frac{1}{\sqrt{2\pi}}\int_{-\infty}^{\infty} dv_\parallel\, v_\parallel^l\; e^{-\frac{v_\parallel^2}{2}\;\left(\frac{v_{thi}}{v_{the}}\right)^2}\sum_{p=0,\pm 1}\frac{\mathcal{N}(p,p')}{\mathcal{D}(m',p)}\Bigg|_{p'=p-m+m'}\;. \tag{34a}$$

Remark that ${\mathcal{I}}^{\,1\;el.}$ only contains the contribution $p = p' = 0$. The numerator $\mathcal{N}(p,p')$ and denominator $\mathcal{D}(m',p)$ in the integrand are defined as:

$$\mathcal{N}(0,0) = \omega_{ne}\left[1+\frac{\eta_e}{2}\left(v_\parallel^2\left(\frac{v_{thi}}{v_{the}}\right)^2 - 1\right)\right] - \omega\;; \tag{34b}$$

$$\mathcal{N}(0,p'=\pm 1)\equiv\mathcal{N}(p=\pm 1,0)=-sign(p)\,\frac{k_\perp\rho_{Le}\,q_s\,v_{the}}{2\,v_\parallel\,v_{thi}} \tag{34c}$$

$$\cdot\left\{\omega_{ne}\,\eta_e\left[2+v_\parallel^2\left(\frac{v_{thi}}{v_{the}}\right)^2\right]+\left[\omega_{ne}\left(1+\frac{\eta_e}{2}\left(v_\parallel^2\left(\frac{v_{thi}}{v_{the}}\right)^2-3\right)\right)-\omega\right]\left[1+v_\parallel^2\left(\frac{v_{thi}}{v_{the}}\right)^2\right]\right\}\;;$$

$$\mathcal{D}(m',p)=\omega-(nq_s-m'-p)\;\bar{\omega}_{ti}\,v_\parallel. \tag{34d}$$

3. Trapped electrons

Non-adiabatic trapped electron dynamics is described by means of a bounce-averaged drift-kinetic equation [17], since the electron bounce frequency is large with respect to the frequency of the perturbation; furthermore FLR as well as finite banana width effects are neglected. Note that owing to the average over the bounce motion, the terms containing $v_\parallel A_\parallel$ cancel, therefore electromagnetic effects do not enter in the contribution of the trapped particle population. Trapped electrons are hence modelled throughout this work as in the electrostatic case [equations 42-45][13].

4. Shafranov shift effects

The Shafranov shift has been taken into account in the present work by considering an equilibrium of circular shifted magnetic surfaces, hence modifying the magnetic flux and the particle trajectories, accordingly to the solution of the Grad-Shafranov equation. One would like to point out that the Shafranov shift is therefore not modelled in this work through the usual standard "$s-\alpha$" model [9], where s represents the magnetic shear and α the so-called ballooning parameter, i.e. the radial derivative of the Shafranov shift.
The Grad-Shafranov equation is given for the case of an axisymmetric equilibrium:

$$\triangle\psi-\frac{2}{r}\frac{\partial\psi}{\partial r}=-\left(I\frac{\partial I}{\partial\psi}+\mu_0\,r^2\frac{\partial p}{\partial\psi}\right)\;; \tag{35}$$

where ψ is the poloidal flux, I is the toroidal flux and p is the plasma pressure.
For the case of a circular cross-section one can conveniently introduce the Shafranov shift through the modified coordinates $r=R+\triangle\,(\rho)+\rho\cos\theta\;,z=-\rho\sin\theta$, where the radial variation $\triangle\,(\rho)$ represents the outward shift of the magnetic surface; $\triangle\,(0)=0$. Assuming the poloidal flux to be a function only of the radial variable, $\psi=\psi(\rho)$ and assuming also

$\triangle' \doteq (d\ \triangle\ /d\rho) \gg \rho/R$, but $\triangle' \sim \rho$ (assumption justified by the solution), one can expand the LHS retaining only terms linear in ρ :

$$\triangle\psi - \frac{2}{r}\frac{\partial\psi}{\partial r} \approx (1 - 2\ \triangle' \cos\theta)\frac{\partial^2\psi}{\partial\rho^2} + \frac{1}{\rho}\frac{\partial\psi}{\partial\rho}[1 - (\triangle' + \rho\ \triangle'')\cos\theta] + \mathcal{O}(\rho^2)\ . \tag{36}$$

Furthermore, since one is considering a low-pressure plasma, one can assume $I\partial I/\partial\psi \sim const.$ and $\partial p/\partial\psi \sim const.$ and approximate the RHS of (35) as :

$$-\left(I\frac{\partial I}{\partial\psi} + \mu_0 r^2\frac{\partial p}{\partial\psi}\right) \approx \mu_0 j_\varphi R - 2\mu_0\,\rho R\,\frac{\partial p}{\partial\psi}\cos\theta + \mathcal{O}(\rho^2)\ . \tag{37}$$

Recombining (36) and (37) one obtains the solution of the Grad-Shafranov equation, for the considered equilibrium:

$$\psi = \frac{\mu_0}{4}\, j_\varphi\, R\, \rho^2\ ; \tag{38a}$$

$$\triangle' = \frac{1}{j_\varphi}\ \frac{\partial p}{\partial\psi}\ \rho\ . \tag{38b}$$

The radial derivative of the Shafranov shift can be finally written as

$$\triangle' = \frac{\mu_0}{2}\ R\frac{dp}{d\rho}\frac{{q_s}^2}{{B_\varphi}^2}\ . \tag{39}$$

Remark that the above parameter differs by a factor $\mu_0/2$ with respect to the usual definition of the so-called ballooning parameter α ; whereas the present calculation coincides with [4]. The equations of the motion for the gyrocenters are evidently modified by the inclusion of the Shafranov shift; after some algebra, they can be rewritten as follows:

$$\begin{aligned}
\dot\rho &\simeq -\frac{v_{dz}\,\sin\theta}{1+\ \triangle'\cos\theta}\ , \\
\dot\theta &\simeq -\frac{1}{1+\ \triangle'\cos\theta}\left[\omega_t + \frac{v_{dz}\,\cos\theta}{\rho}(1+\ \triangle'\cos\theta)\right]\ , \\
\dot\varphi &\simeq \frac{v_\parallel}{R}\ .
\end{aligned} \tag{40}$$

In the present work the Shafranov shift has been taken into account only for the circulating particle population, therefore one can assume $v_\parallel = const.$ and derive the trajectories of the gyrocenters for passing particles. The poloidal component is solved iteratively, considering the drift as a higher order term, $\dot\theta \equiv \dot\theta_0 + \dot\theta_1$. At the first order in $\triangle'$, one obtains

$$\theta_0\ \simeq -\,\omega_t\, t + \triangle'\sin(\omega_t\, t)\ ; \tag{41a}$$

$$\theta_1\ \simeq -\frac{\zeta}{\rho}\left[\sin(\omega_t\, t) + \frac{\triangle'}{2}\omega_t\, t\right]\ ; \tag{41b}$$

where one defined $\zeta \doteq v_{dz}/\omega_t$. The radial and toroidal component give instead

$$\rho \;=\; -\,\zeta\cos(\omega_t\,t)\;, \tag{41c}$$

$$\varphi \;=\; \frac{v_\parallel}{R}\,t\;. \tag{41d}$$

Equations (41) represent the modified trajectories for guiding centers of passing particles, including the Shafranov shift effect. Introducing these trajectories in the general expression of the propagator (15), one can obtain an explicit expression for the electromagnetic gyrokinetic equation which takes into account the Shafranov shift.

Since we are considering circulating particles, the frequency of the periodic motion, corresponds to the transit frequency, ω_t. Substituting in (13), (14):

$$g(t) \;=\; \frac{v_\parallel}{R}\left[n - \frac{m}{q_s}\left(1+\zeta\,\frac{\triangle'}{2\rho}\right)\right]\,t + \tilde{g}(t)\;, \tag{42a}$$

$$\tilde{g}(t) \;=\; -\,\kappa\,\zeta\;\cos\left(\omega_t\,t\right) - m\left(\frac{\zeta}{\rho} - \triangle'\right)\sin\left(\omega_t\,t\right) \equiv \xi\sin\left(\omega_t\,t-\bar{\theta}\right)\;, \tag{42b}$$

$$\begin{aligned} a_p \;&=\; \frac{1}{\tau}\int_0^\tau dt\;\exp i\left[\xi\sin\left(\omega_t t-\bar{\theta}\right) - p\,\omega_t t\right] = \frac{1}{2\pi}\int_0^{2\pi} d\vartheta\;\exp i\left[\xi\sin\left(\vartheta-\bar{\theta}\right) - p\,\vartheta\right] \\ &\equiv\; J_p(\xi)\;e^{-ip\,\bar{\theta}}\;\;; \end{aligned} \tag{42c}$$

where use has been made of the integral representation of Bessel function J_p and of the definitions

$$\xi \doteq \zeta\;\left[\kappa^2 + \frac{m^2}{\rho^2}\left(1-\frac{\rho\,\triangle'}{\zeta}\right)^2\right]^{1/2}\;,\;\tan\bar{\theta} \doteq -\,\frac{\kappa}{\frac{m}{\rho}\;\left(1-\frac{\rho\,\triangle'}{\zeta}\right)}\,.$$

Finally the propagator (15), assumes the explicit expression:

$$e^{i\,\omega\,t}\;\mathcal{P} = i\sum_{p,p'}\;\frac{a_p\,a^*_{p'}\;e^{-i\,(p-p')\,\theta}}{\omega - \left[nq_s - m\left(1+\zeta\;\frac{\triangle'}{2\rho}\right) - p\right]\;\omega_t}\;\;. \tag{43}$$

Remark that the Shafranov shift enters in the argument of the Bessel functions, through the modified poloidal wavevector $k_\theta \to k_\theta(1-\rho\;\triangle'\;/\zeta)$; whereas the parallel wavevector is modified as follows, $k_\parallel \to [nq_s - m(1+\zeta\;\triangle'\;/2\rho)]/q_s R$. In those terms, ζ is further approximated to $\zeta \simeq sign(q_j)\;2\,q_s\,\rho_{Lj}$. Also remark that to be consistent with the approximations made, the correction to k_θ needs to be small; in particular, one has to ensure that the condition allowing for the drift-kinetic electron approximation, $k_\perp\rho_{Le} \ll 1$, is still fulfilled.

III. NUMERICAL IMPLEMENTATION AND CODE VALIDATION

The numerical implementation is carried out in an way analogous to the electrostatic case [13], the major modifications of the model being the inclusion of the parallel vector potential, of the parallel Ampère's law and of non-adiabatic electron dynamics, as already mentioned. The 2D eigenvalue system is solved in Fourier space (κ, m), where it is already discretized and cast into matrix form (20). For the numerical implementation one simply needs to reduce the infinite system to a finite number of significant matrix elements. An equidistant radial mesh of n_ρ points is chosen, so that the integrations over ρ are numerically performed by applying a Fast Fourier Transform (FFT). The coupling between radial mode numbers is taken into account only for $|\kappa - \kappa'| \lesssim n_\rho/2$, so that each of the four submatrices of $\mathcal{M}^{tot}_{\vec{k},\vec{k}'}$, is a band matrix. The coupling between poloidal components and the appropriate order of transit frequency harmonics to be included is evaluated as in the electrostatic case, for the ion contribution. For electrons only the coupling between neighboring poloidal mode numbers $\Delta m = \pm 1$ is taken into account; whereas only the fundamental and first harmonic of the electron transit frequency are kept, since $\omega, \omega_{ne} \ll \bar{\omega}_{te}$, as commented in section II A 2. The velocity integrations are carried out by means of an extended trapezoidal rule on equidistant meshes. A critical point, is the numerical resolution of the denominators of the electron parallel velocity integrals, equations (34), since the radial behavior of such integrals around rational surfaces presents very steep gradients, thus requiring a fine radial mesh and introducing large radial wave-numbers. This is more evident remarking that, after some algebra, these integrals can be written in terms of plasma dispersion functions [18] of argument $z \equiv (\omega/k_\parallel v_{the})$:

$$\mathcal{W}(z) = \frac{1}{2\pi} \int_{-\infty}^{\infty} dx \, \frac{x}{x - z} \, e^{-x^2/2}. \tag{44}$$

Around $k_\parallel = 0$, i.e. around rational surfaces, the argument varies from very large values to values such that $|\,\omega/k_\parallel v_{the}| \ll 1$, consistent with the chosen electron frequency ordering. The smaller the ratio $|\,\omega/v_{the}|$, the shorter the scale on which that variation occurs. Observing the asymptotic expansion of the plasma dispersion function for large z, $\mathcal{W}(z) \simeq -1/z^2 - \mathcal{O}(1/z^4)$, whereas for $|\,z| < 1$, $\mathcal{W}(z) \simeq 1 - z^2 + \mathcal{O}(z^4)$, it is clear that the variation from one expansion to the other produces sharp gradients.

A. Solving for the eigenfrequencies

The search for the zeros of $\det \mathcal{M}(\omega)$ is carried out by either sampling the determinant over a Cartesian mesh grid in the complex ω-plane or taking advantage of its analyticity, by using a higher order Nyquist algorithm [19], [20]. The latter method is the most advantageous since the number of frequency evaluations required per enclosed eigenfrequency is typically 10-20, compared to a few hundreds for a scan in the complex plane. Both the approaches can easily be implemented on a parallel machine.

The parallel implementation has been carried out on the Silicon Graphics Origin 3000 of the EPFL, involving 10 or 32 of its 128 R14000 processors (operating at 500 Mhz). Use is made of MPI Fortran90 Library. The typical computing time for the construction of the matrix and the evaluation of the determinant is ~ 20 minutes per frequency and per processor. Whereas the eigenmode computation requires ~ 20 minutes of CPU time on an Intel Pentium III operating at 1GHz.

B. Eigenmode structure analysis

Different physical quantities are evaluated by means of averages over the eigenmode $\vec{\Phi}(\rho,\theta)$. Generalizing [13, page 3940], the average components of the wavevector $\vec{k}$ are evaluated as follows:

$$< k_\rho^2 >= \frac{\sum_{(k,m)} \left(|\kappa\, \hat{\phi}_{(k,m)}|^2 + |\kappa\, \hat{A}_{\|(k,m)}|^2 \right)}{\sum_{(k,m)} |\hat{\phi}_{(k,m)}|^2 + \sum_{(k,m)} |\hat{A}_{\|(k,m)}|^2} \,, \tag{45a}$$

$$< k_\theta^2 >= \frac{\int_{\rho_l}^{\rho_u} d\rho \sum_m |\frac{m}{\rho}\, \hat{\phi}_m|^2 + \int_{\rho_l}^{\rho_u} d\rho \sum_m |\frac{m}{\rho}\, \hat{A}_{\|m}|^2}{\int_{\rho_l}^{\rho_u} d\rho \sum_m |\hat{\phi}_m|^2 + \int_{\rho_l}^{\rho_u} d\rho \sum_m |\hat{A}_{\|m}|^2} \,, \tag{45b}$$

$$< k_\perp^2 >=< k_\rho^2 > + < k_\theta^2 > \,; \tag{45c}$$

where $\hat{\phi}_m \equiv \hat{\phi}_m(\rho) = \sum_k \hat{\phi}_{(k,m)} e^{i\kappa\rho}$ is the radial dependence of the poloidal Fourier component m. The mean square radial width of the modes is instead evaluated as:

$$(\Delta s)^2 = \frac{\sum_{(k,m)} \left(|s\, \hat{\phi}_{(k,m)}|^2 + |s\, \hat{A}_{\|(k,m)}|^2 \right) - \left[\sum_{(k,m)} \left(s\, |\hat{\phi}_{(k,m)}|^2 + s\, |\hat{A}_{\|(k,m)}|^2 \right) \right]^2}{\sum_{(k,m)} |\hat{\phi}_{(k,m)}|^2 + \sum_{(k,m)} |\hat{A}_{\|(k,m)}|^2} \,. \tag{46}$$

Finally, a diagnostic on the electromagnetic character of the modes is provided by computing the ratio of the normalized parallel vector potential to the electrostatic potential:

$$\frac{< A_{\parallel}^2 >}{< \phi^2 >} = \frac{\sum_{(k,m)} |\hat{A}_{\parallel(k,m)}|^2}{\sum_{(k,m)} |\hat{\phi}_{(k,m)}|^2} \, . \tag{47}$$

C. Benchmarking

The validity and accuracy of the original electrostatic code GLOGYSTO had been established through a rigorous benchmark with a linear, time evolution PIC code [13, 21]. For the present electromagnetic extension one has been restrained to benchmark the global code against a local kinetic dispersion relation, derived as in [5], modelling also trapped electrons. This comparison has provided a good qualitative agreement, nonetheless the local simulations predict a stabilization of the ITG mode at almost half of β threshold given by global simulations and overestimate the electromagnetic mode growth rates and frequencies (respectively by a factor $2 - 2.5$, $1.3 - 1.8$).

IV. RESULTS

The global numerical simulations presented here have been performed choosing a hydrogen toroidal plasma having the following magnetic geometry $B_0 = 1.\,\mathrm{Tesla}, R = 2.\,m, a = 0.5\,m$, with safety factor profile $q_s(s) = 1.25 + 0.67s^2 + 2.38s^3 - 0.06s^4$, $s = \rho/a$ being the normalized radial variable; $q_s(s_0) = 2$ and magnetic shear $\hat{s}(s_0) = 1$, at $s_0 = 0.6$. The density profile and the identical electron and ion temperature profiles have been chosen of the form

$$\frac{f(s)}{f(s_0)} = \exp\left(-\frac{a\Delta s}{L_0}\tanh\frac{s - s_0}{\Delta s}\right) ,$$

Δs defining the radial width of the profiles and L_0 the characteristic scale length of variation at s_0; $\Delta s_n = 0.35,\ L_{n0} = 0.4\,m,\ \Delta s_T = 0.20,\ L_{T0} = 0.2\,m,\ T(s_0) = 7.5\,KeV$. The density $N(s_0)$ is evaluated from the value of $\beta(s_0)$; by definition $\beta = 2\mu_0 N(T^e + T^i)/B_0^2$.
Frequencies are normalized to $\omega_{norm} = \rho_{Li}(0)\, v_{thi}(0)/a^2 \simeq 3 \cdot 10^4$ Hz.

A. Finite β effects on ITG and AITG modes.

One of the main interests of this work was to provide evidence for the appearance of the new branch of electromagnetic modes, KBM or AITG, which, as already mentioned, had been predicted in previous works [3], [10] to be destabilized by electromagnetic effects, to have a frequency much higher than the ITG but lower than the Alfvén wave frequency and to be localized around some magnetic surface.

1. β scan

First, a scan over the parameter β, up to $\beta(s_0) = 7\%$ has been carried out, considering the toroidal mode number $n = 7$. Note that a scan over the parameter β corresponds to a scan over density. The results, presented in Figure 1, show that at approximately half the value of β for which the stabilization of the ITG mode occurs, another mode is destabilized. The growth rate of this mode rises rapidly, overcoming the ITG maximal growth rate already at $\beta \simeq 1.5\%$, whereas its frequency is initially 6 times larger than the ITG's and decreases significantly with β. Note that the difference of frequencies in the region where the two modes coexist is smaller than one order of magnitude, value that had been observed in ballooning simulations [3],[8]; one can anyway agree that the ITG and the new electromagnetic mode, AITG, are not different eigenstates of the same instability branch.
Remark that only the most unstable electromagnetic mode has been followed in the scan, but the spectrum contains also other modes, having a more slab character, which can become more unstable in certain parameter regions.
The mode structure analysis shows that the AITG mode is most predominantly electromagnetic and is not radially localized around the magnetic surface where the temperature gradients are maximum, but around inner rational surfaces, where incidentally β is higher. Figure 2 shows a typical AITG mode radial structure, both in Fourier space (top plots) and in configuration space (bottom plots), for $\beta(s_0) = 6\%$; the mode components are labelled with the value of the poloidal mode number. One can notice that in Fourier space the electrostatic potential presents a much wider k_r spectrum than the vector potential. Remark that the convergence of the mode in Fourier space does not improve increasing the number of radial Fourier components taken into account, since, as discussed in section III high

radial components are introduced by the high variations of the electron velocity integrals on very short radial scales. In configuration space one can observe that the poloidal mode decomposition does not present a smooth envelope as it happens for toroidal ITG modes; modulations on small radial scales are appearing due to high radial wavenumbers produced by electron dynamics, as mentioned above. One can observe the expected resonant behavior of the potential poloidal components: for the electrostatic potential their amplitude is maximal near the corresponding rational surfaces, whereas, the poloidal components of the parallel vector potential tend to vanish at the magnetic surface for which $k_{\|}(s,m) = 0$.

2. Toroidal mode number scan

A scan over the toroidal mode number has been carried out in order to identify the maximum growth rate for AITG modes; in particular, the two most unstable electromagnetic modes at $n = 7$ have been followed throughout the scan, fixing $\beta(s_0) = 6\%$. One can observe, from the results presented in Figure 3, that the role of the most unstable mode can be interchanged depending on the n value; precisely the second unstable mode at $n = 7$, labelled "mode 2", overcomes "mode 1" for $n \geq 8$.

The average value of $k_\theta \rho_{Li} = n q_s \rho_{Li}/\rho$, corresponding to each n is reported on the top axis. The scan performed for the AITG mode with our global electromagnetic code shows that this electromagnetic mode tends to peak at $n = 6$, which, for the chosen parameters, corresponds to a value of $k_\theta \rho_{Li} = 0.35$.

The ratio of parallel vector potential to electrostatic potential (both square averaged over the mode), is plotted in Figure 4 for the AITG "mode 1", showing that low n modes, which are more extended in the poloidal plane and have lower growth rates, are more electromagnetic. Figure 5 shows the average radial position of the same AITG mode, versus the toroidal mode number; also drawn is the mean square radial width, Δs, evaluated by (46). One can observe that the mean radial width of the AITG modes does not vary much with n; besides, for almost all the values of n, the average radial position lies inside the magnetic surface $s_0 = 0.6$ where η profiles peak. In Figure 6 the average wavevector components for the AITG "mode 1" are drawn versus the toroidal mode number; the values averaged over the eigenmode structure have been computed through (45). Remark that the perpendicular wavevector increases with k_ρ; this scaling is different from what is observed for toroidal ITG

modes where $k_\perp$ is shown to scale with k_θ [11],[13]. A mixing length estimate of the diffusion coefficient has been evaluated through the relation $D_{ML} = \gamma / < k_\perp >^2$, always for the AITG mode 1 of Figure 3; the computed values are presented in Figure 7 as a function of n.

B. Effect of trapped electron dynamics

The scan over β has been repeated including trapped electron dynamics, always for the toroidal wave number $n = 7$. First, the effect of trapped electrons on ITG modes is analyzed. It is shown that the coupling to trapped electrons produces an increase in the growth rates of ITG modes, more pronounced at low β, though the stabilizing effect of finite β is still dominant. It is evident from Figure 8, that the threshold for the stabilization of ITG modes coupled to trapped electrons (full grey line) is slightly increased. For what concerns trapped electron modes (TEM) they are instead found not to be affected by increasing β [16].
The effect of trapped electrons on the stability of the AITG modes had not been analyzed in previous works. From a local electromagnetic dispersion relation computations, they were expected to induce a decrease of the mode growth rates; on the contrary, the global electromagnetic code simulations have shown that non-adiabatic trapped electron dynamics further destabilizes the electromagnetic modes. The global results presented in Figure 8 besides show that a second unstable mode can eventually be dominant, for some values of β. The two coupled AITG - trapped electron modes have been labelled in the viewgraph as "mode 1 TE" and "mode 2 TE", the first being the most unstable electromagnetic mode at high β. The plot also reports for comparison the AITG mode without trapped electrons (full line with triangles). It is interesting to observe that the growth rate of the most unstable AITG mode coupled to trapped electrons does not exceed that of the coupled ITG-trapped electron mode at zero β limit. One can conclude that when electromagnetic effects are taken into account, the presence of trapped electrons further destabilizes the existing modes, hence there is a very narrow interval in β in which the instabilities are weak.
The coupling of AITG modes to trapped electrons lowers the ratio of the potentials for both modes, as depicted in Figure 9. Some radial structures in the configuration space of the AITG mode coupled to trapped electrons, "mode 1" of fig. 8, are shown in Figure 10, for different values of β; the corresponding structures in the poloidal plane are presented in Figure 11. Remark that for increasing β the ballooning character of the mode is more

pronounced and its radial extension is wider; moreover depending on the value of β the AITG modes are centered around different magnetic surfaces.

C. Effect of the Shafranov shift

Always considering a toroidal mode number $n = 7$, the scan over β has been repeated taking into account the Shafranov shift and including this time only circulating particle dynamics, since this effect has not been implemented to the trapped electron trajectories. Results are depicted in Figure 12. One can observe that the inclusion of the Shafranov shift engenders a very strong stabilization of toroidal ITG modes, since it is already effective at very low values of β. The threshold for the stabilization occurs at a value of $\beta \simeq 0.5\%$, corresponding to a factor 10 lower than the value obtained considering only the electromagnetic perturbation. Concerning the AITG modes, to ensure that the correction introduced by the Shafranov shift on the poloidal wavevector would be sufficiently small, computations have been performed including 5% of the Shafranov shift value, $\triangle'$. Results, also reported in Figure 12, show a stabilization of the electromagnetic modes [22]; it is evident that the growth rate of the AITG mode is halved. Contours of the ITG mode potentials in the poloidal plane are collected in Figure 13, in the unshifted magnetic surfaces frame. One can remark that the modes are not centered in the circular section, but are shifted upwards and outwards. The parallel vector potential is radially more extended than in the case without Shafranov shift, presenting long "fingers", while the ballooning structure is still preserved.

V. DISCUSSION AND CONCLUSIONS

An in-depth numerical investigation of the properties of electromagnetic microinstabilities in toroidal plasmas has been carried out by means of a global electromagnetic gyrokinetic spectral code. It is found that finite β effects on ITG modes are stabilizing, even when the ITG is coupled to trapped electrons. In agreement with previous works, it is also found that there exist a threshold in β above which a new branch of electromagnetic modes is driven unstable, whilst there is a regime in which the two modes coexist. It is shown that the electromagnetic mode, AITG, is driven by thermal gradients of both ions and electrons and that the coupling of AITG modes to trapped electrons leads to a further destabilization of

the mode. Finally, a scan over the toroidal mode number has allowed one to observe that the AITG mode growth rates peak at $k_\theta \rho_{Li} \simeq 0.35$, for the considered parameters. The use of the global model has furthermore allowed one to first disclose the radial structure of the electromagnetic AITG modes, which are shown to present small scales due to the electron dynamics and a resonant behavior of the potentials poloidal components around rational surfaces. Analyses of the mode structure in the poloidal plane has instead allowed one to observe that this electromagnetic mode conserves a ballooning structure, more pronounced for the parallel vector potential.

Comparisons with simulations from a local dispersion relation have only shown a qualitative agreement, largely overestimating the electromagnetic mode growth rates and predicting an opposite effect for the coupling of AITG modes to trapped electrons. This underscores the need of global simulations for providing a good description of the electromagnetic mode behavior.

The successive inclusion of the Shafranov shift in the model has enabled a distinction to be made among the effects of finite β, namely between the consequences of the electromagnetic perturbations from those of the modified geometry, whereas previous works using the "s-α" model could not allow for such a distinction. Results have shown that, the Shafranov shift is responsible for an even stronger stabilization of the toroidal ITG modes than that due to the sole effect of the electromagnetic perturbation. Precisely, in the parameter regime analyzed here, one has observed a decrease of a factor $\simeq 10$ of the β threshold for the stabilization of toroidal ITG modes. A stabilizing effect is also observed on the electromagnetic modes.

A further extension of the present work will be the inclusion of the $\vec{E} \times \vec{B}$ flow, which had been implemented in the electrostatic version of the code [23], both for circulating and trapped particles. Whereas a gyrokinetic description of electrons will allow one to exploit the code also for the study of Electron Temperature Gradient (ETG) driven modes.

Comparisons with the linear phase of existing non-linear electromagnetic codes will be a high priority in the future, though at present most of the non-linear gyrokinetic models can only describe the physics of toroidal ITG modes [24] or ETG modes [25].

Acknowledgments

We are grateful to X. Garbet, T.S. Hahm, F. Cheng and F. Zonca, for stimulating questions and elucidating discussions. This work was supported in part by the Swiss National Science Foundation. The computations were performed on the Origin3000 of the Ecole Polytechnique Fédérale de Lausanne.

[1] W. Tang, J. Connor, and R. J. Hastie, Nuclear Fusion **21**, 1439 (1980).

[2] C. Z. Cheng, Physics of Fluids p. 1020 (1982).

[3] J. Dong, L. Chen, and F. Zonca, Nuclear Fusion **39**, 1041 (1999).

[4] B. Coppi, A. Ferreira, J. W. K. Mark, and J. J. Ramos, Nuclear Fusion **19**, 715 (1979).

[5] J. Kim, W. Horton, and J. Dong, Physics of Fluids B **5**, 4030 (1993).

[6] B.-G. Hong, W. Horton, and D.-I. Choi, Physics of Fluids B **1**, 1589 (1989).

[7] P. B. Snyder and G. W. Hammett, Physics of Plasmas **8**, 744 (2001).

[8] F. Zonca, L. Chen, J. Dong, and R. A. Santoro, Physics of Plasmas **6**, 1917 (1999).

[9] J. Connor, R. Hastie, and J. Taylor, Physical Review Letters **40**, 396 (1978).

[10] H. Qin, W. M. Tang, and G. Rewoldt, Physics of Plasmas **6**, 2544 (1999).

[11] W. M. Tang and G. Rewoldt, Physics of Fluids B **5**, 1164 (1993).

[12] S. Brunner, thesis 1701, Ecole Polytechnique Fédérale de Lausanne, Switzerland (1997).

[13] S. Brunner, M. Fivaz, T. Tran, and J. Vaclavik, Physics of Plasmas **5**, 3929 (1998).

[14] P. Catto, W. M. Tang, and D. E. Baldwin, Plasma Physics **23**, 639 (1981).

[15] B. Coppi, M. Rosenbluth, and P. Rutherford, Physical Review Letters **21**, 1055 (1968).

[16] G. L. Falchetto and J. Vaclavik, *Theory of Fusion Plasmas, Proc. Int. Workshop, Varenna, August 2000* (Editrice Compositori, Società Italiana di Fisica, Bologna, 2000), p. 321.

[17] M. Rosenbluth, Physics of Fluids **11**, 869 (1968).

[18] S. Ichimaru, *Basic Principles of Plasma Physics - A statistical approach* (W. A. Benjamin, Inc., London, 1973).

[19] B. Davies, Journal of Computational Physics **66**, 36 (1986).

[20] S. Brunner and J. Vaclavik, Physics of Plasmas **5**, 365 (1998).

[21] M. Fivaz, thesis 1692, Ecole Polytechnique Fédérale de Lausanne, Switzerland (1997).

[22] G. L. Falchetto and J. Vaclavik, *to be published in Proc. 29th EPS* (2002), vol. 26B, p-5.061.

[23] M. Maccio, J. Vaclavik, and L. Villard, Physics of Plasmas **8**, 895 (2001).

[24] Z. Lin, T. S. Hahm, W. W. Lee, W. M. Tang, and R. B. White, Science **281**, 1835 (1998).

[25] F. Jenko, W. Dorland, M. Kotschenreuther, and B. N. Rogers, Physics of Plasmas **7**, 1904 (2000).

Figure Captions

FIG. 1. Growth rates and real frequencies of the ITG mode (dashed line) and of the electromagnetic mode, AITG or KBM (full line), versus $\beta(s_0)$. Frequencies are normalized with respect to $\omega_{norm} \simeq 3 \cdot 10^4$ Hz.

FIG. 2. Poloidal mode decomposition in Fourier space(a-b) and in configuration space(c-d) for the electrostatic potential ϕ and normalized parallel vector potential $A_\parallel$ of the AITG mode at $\beta = 6\%$, figure 1. On the top axis the positions of mode rational surfaces are reported.

FIG. 3. Normalized growth rates and real frequencies of the AITG mode for $\beta(s_0) = 6\%$, as a function of the toroidal wave number n. On the top axis the corresponding average value of $k_\theta \rho_{Li}$ is reported. The full line represents the most unstable electromagnetic mode for $n = 7$, while the dashed line shows a second unstable mode, "mode 2".

FIG. 4. Ratio of the square averaged parallel vector potential over the electrostatic potential, of the AITG "mode 1", of Figure 3, for $\beta(s_0) = 6\%$, as a function of the toroidal mode number n.

FIG. 5. Average radial position $< s >$ (full line) and mean square width (dotted lines) of the AITG "mode 1", as a function of the toroidal mode number n.

FIG. 6. Average values of $k_\perp \rho_{Li}$ (full line), $k_\rho \rho_{Li}$ (dash-dotted line) and $k_\theta \rho_{Li}$(dashed line), as a function of the toroidal mode number n, for the AITG "mode 1", referring to Figure 3.

FIG. 7. Mixing length estimate of the diffusion coefficient $D_{ML} = \gamma \,/\, < k_\perp >^2$ for the AITG "mode 1", as a function of the toroidal mode number n.

FIG. 8. Normalized growth rates and real frequencies, versus $\beta(s_0)$, of the coupled ITG-trapped electron mode (grey full line with $*$) and of two branches of AITG modes coupled to

trapped electrons (dashed line and the dash-dotted line). For comparison the AITG without trapped electrons (full line with triangles) is reported.

FIG. 9. Ratio of the square averaged parallel vector potential and electrostatic potential, as a function of $\beta(s_0)$ for AITG modes (full line), AITG with trapped electrons mode 1 (dashed line, full circles) and mode 2 (dash-dotted line, open squares), referring to Figure 8.

FIG. 10. Radial mode structures of the electrostatic potential Φ (left column) and the vector potential $A_\parallel$ (right column) of AITG modes coupled with trapped electron dynamics ("mode 1 TE" referring to Figure 8), for $\beta(s_0) = 1\%, 3\%, 6\%$ (growing values from top to bottom).

FIG. 11. Poloidal contours of the electrostatic potential Φ (left column) and the vector potential $A_\parallel$ (right column) of AITG modes coupled with trapped electron dynamics ("mode 1 TE" referring to Figure 8), for $\beta(s_0) = 1\%, 3\%, 6\%$ (growing values from top to bottom).

FIG. 12. Normalized growth rates and real frequencies of ITG modes with the Shafranov shift (diamonds) and AITG modes including 5% $\triangle'$ (full line with triangles). ITG and AITG modes computed neglecting the Shafranov shift, are reported for comparison, respectively in dash-dotted line and dashed line with full circles.

FIG. 13. Poloidal contours of the electrostatic potential ϕ (left column) and the vector potential $A_\parallel$ (right column) of ITG modes with Shafranov shift, referring to Figure 12, for two values of β, $\beta(s_0) = 0.1\%$ (top), 0.4% (bottom).

Figures

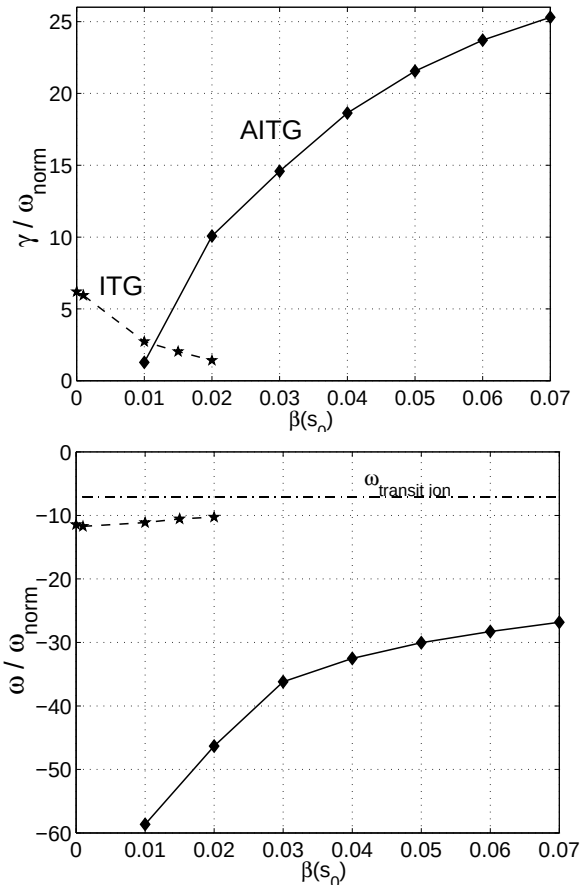

FIG. 1: Growth rates and real frequencies of the ITG mode (dashed line) and of the electromagnetic mode, AITG or KBM (full line), versus $\beta(s_0)$. Frequencies are normalized with respect to $\omega_{norm} \simeq 3 \cdot 10^4$ Hz.

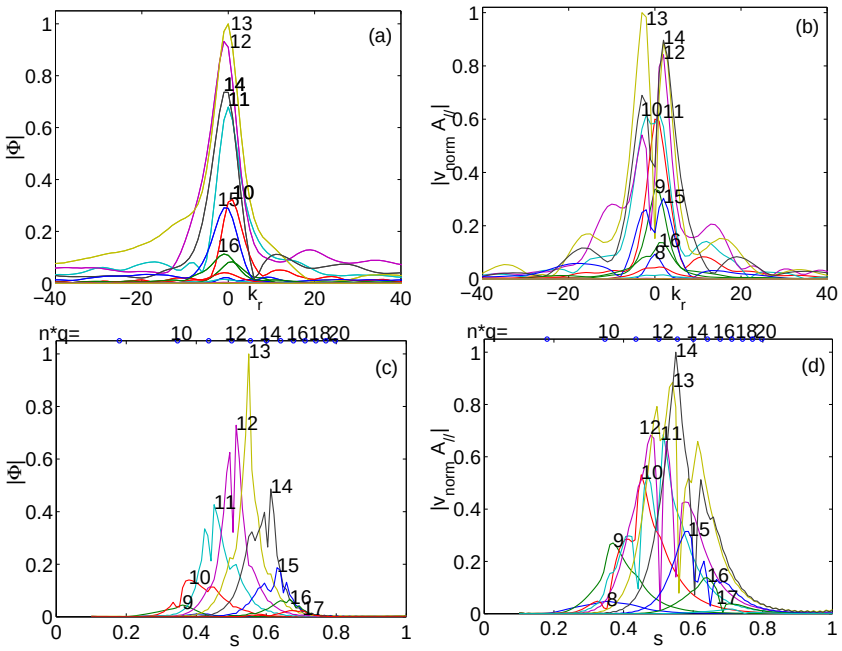

FIG. 2: Poloidal mode decomposition in Fourier space(a-b) and in configuration space(c-d) for the electrostatic potential ϕ and normalized parallel vector potential $A_{||}$ of the AITG mode at $\beta = 6\%$, figure 1. On the top axis the positions of mode rational surfaces are reported.

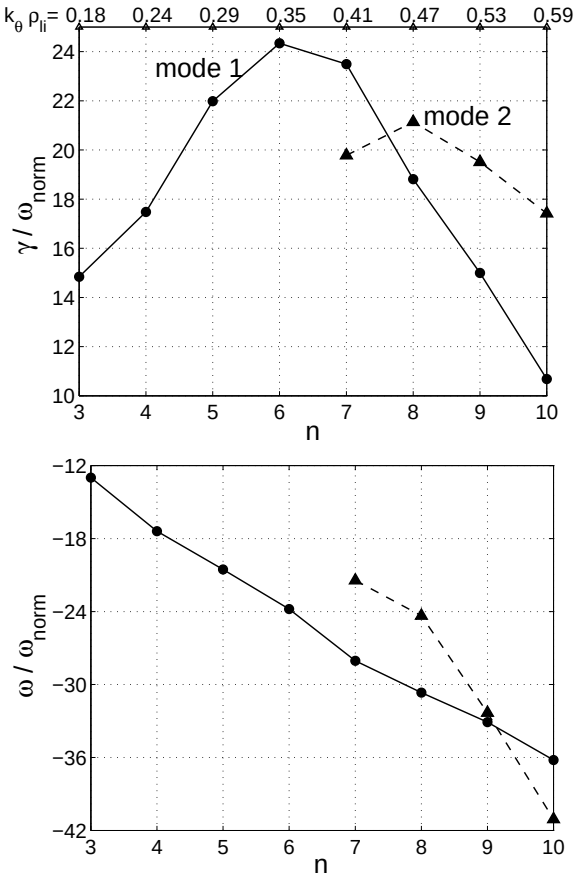

FIG. 3: Normalized growth rates and real frequencies of the AITG mode for $\beta(s_0) = 6\%$, as a function of the toroidal wave number n. On the top axis the corresponding average value of $k_\theta \rho_{Li}$ is reported. The full line represents the most unstable electromagnetic mode for $n = 7$, while the dashed line shows a second unstable mode, "mode 2".

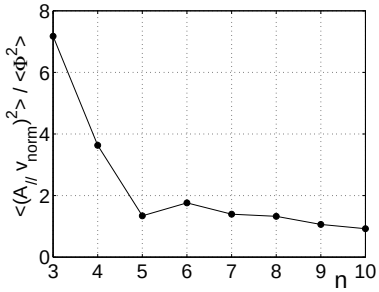

FIG. 4: Ratio of the square averaged parallel vector potential over the electrostatic potential, of the AITG "mode 1", of Figure 3, for $\beta(s_0) = 6\%$, as a function of the toroidal mode number n.

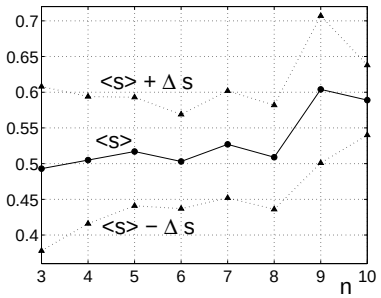

FIG. 5: Average radial position $< s >$ (full line) and mean square width (dotted lines) of the AITG "mode 1", as a function of the toroidal mode number n.

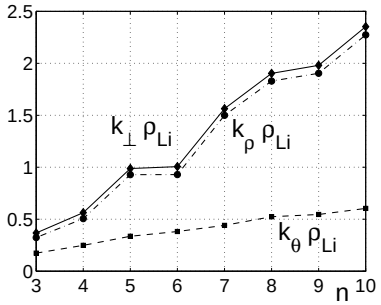

FIG. 6: Average values of $k_\perp \rho_{Li}$ (full line), $k_\rho \rho_{Li}$ (dash-dotted line) and $k_\theta \rho_{Li}$(dashed line), as a function of the toroidal mode number n, for the AITG "mode 1", referring to Figure 3.

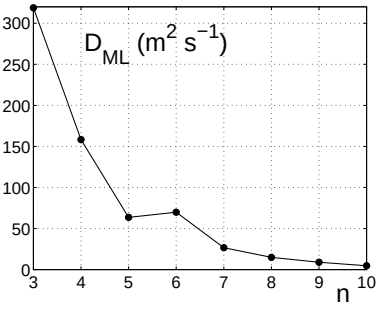

FIG. 7: Mixing length estimate of the diffusion coefficient $D_{ML} = \gamma \, / < k_\perp >^2$ for the AITG "mode 1", as a function of the toroidal mode number n.

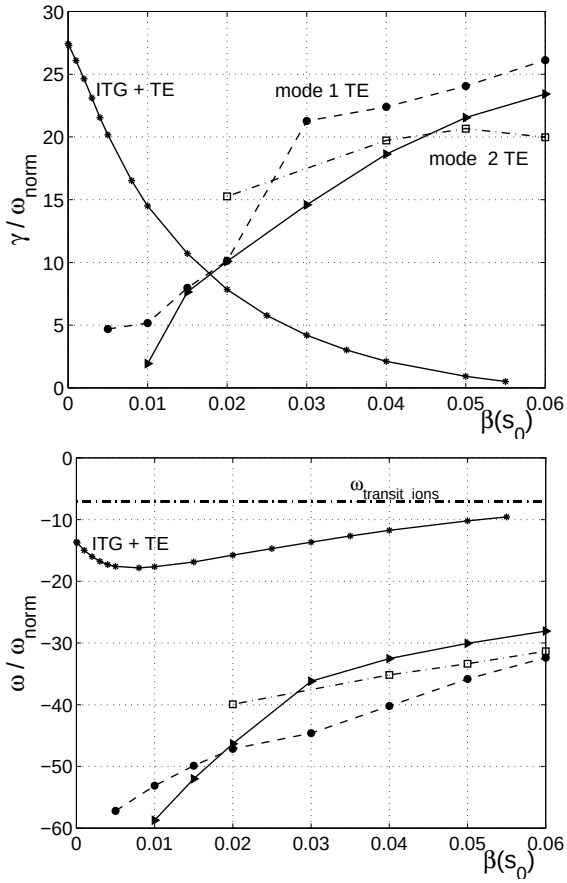

FIG. 8: Normalized growth rates and real frequencies, versus $\beta(s_0)$, of the coupled ITG-trapped electron mode (grey full line with $*$) and of two branches of AITG modes coupled to trapped electrons (dashed line and the dash-dotted line). For comparison the AITG without trapped electrons (full line with triangles) is reported.

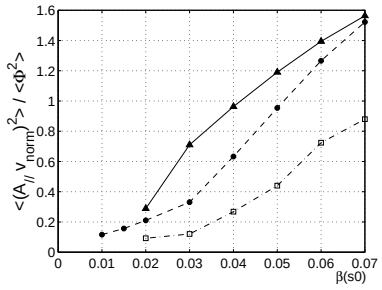

FIG. 9: Ratio of the square averaged parallel vector potential and electrostatic potential, as a function of $\beta(s_0)$ for AITG modes (full line), AITG with trapped electrons mode 1 (dashed line, full circles) and mode 2 (dash-dotted line, open squares), referring to Figure 8.

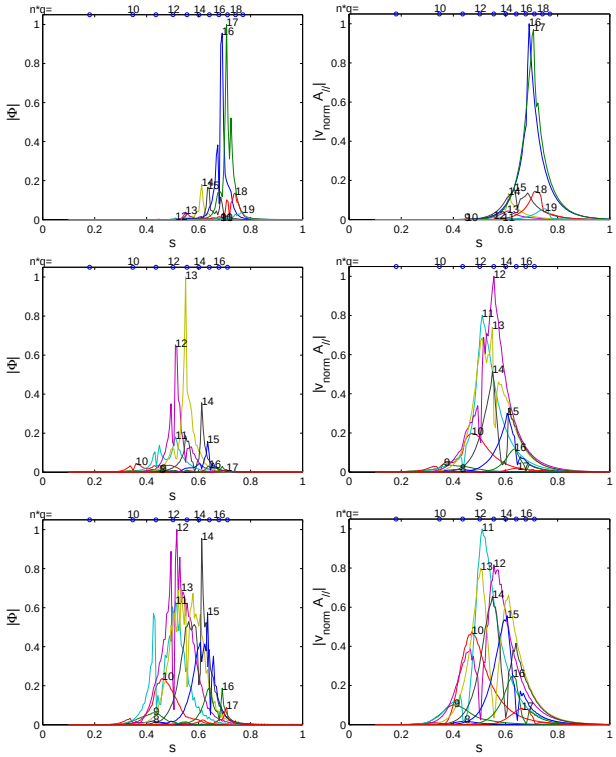

FIG. 10: Radial mode structures of the electrostatic potential Φ (left column) and the vector potential $A_{\|}$ (right column) of AITG modes coupled with trapped electron dynamics ("mode 1 TE" referring to Figure 8), for $\beta(s_0) = 1\%, 3\%, 6\%$ (growing values from top to bottom).

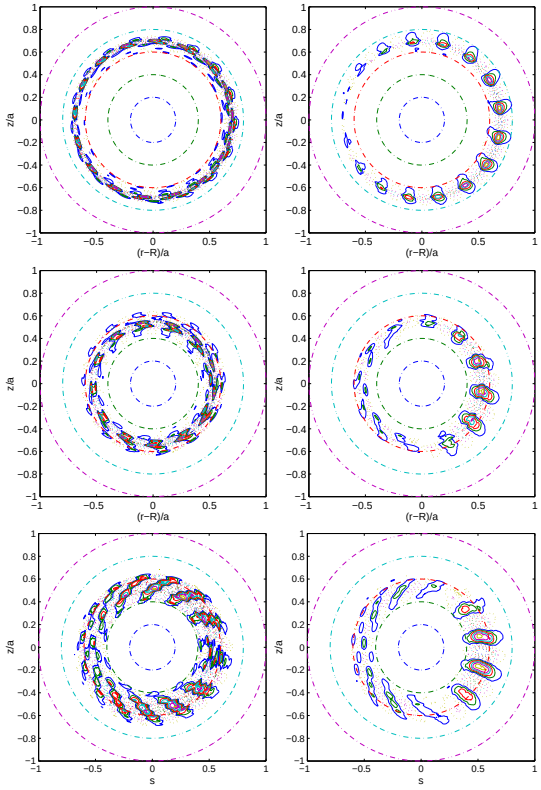

FIG. 11: Poloidal contours of the electrostatic potential Φ (left column) and the vector potential $A_\parallel$ (right column) of AITG modes coupled with trapped electron dynamics ("mode 1 TE" referring to Figure 8), for $\beta(s_0) = 1\%, 3\%, 6\%$ (growing values from top to bottom).

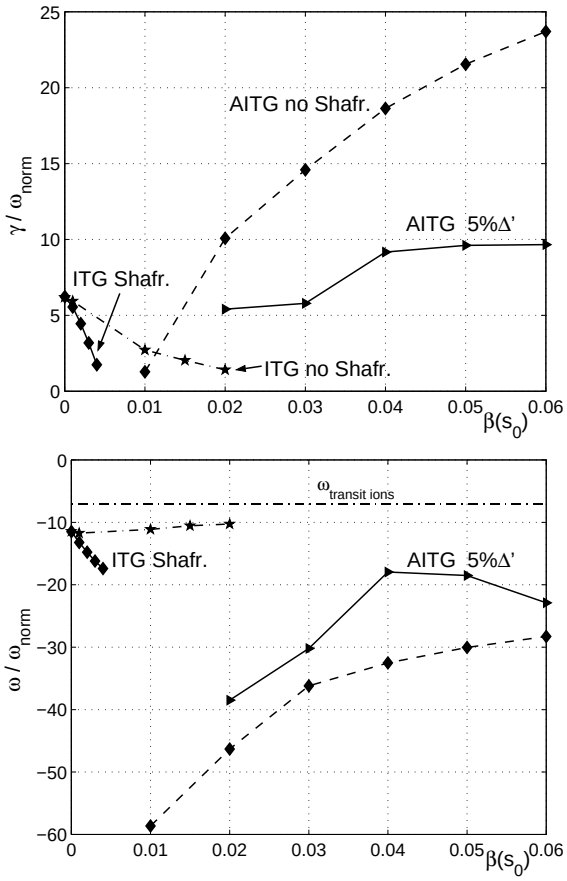

FIG. 12: Normalized growth rates and real frequencies of ITG modes with the Shafranov shift (diamonds) and AITG modes including 5% $\triangle'$ (full line with triangles). ITG and AITG modes computed neglecting the Shafranov shift, are reported for comparison, respectively in dash-dotted line and dashed line with full circles.

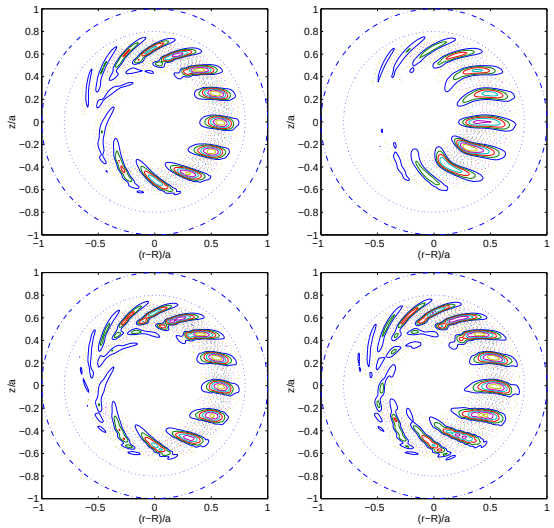

FIG. 13: Poloidal contours of the electrostatic potential ϕ (left column) and the vector potential $A_{\|}$ (right column) of ITG modes with Shafranov shift, referring to Figure 12, for two values of β, $\beta(s_0) = 0.1\%$ (top), 0.4% (bottom).